nature communications

Article

https://doi.org/10.1038/s41467-025-57638-4

Photoisomerization-mediated tunable pore size in metal organic frameworks for U(VI)/V(V) selective separation

Received: 27 February 2024

Accepted: 26 February 2025

Published online: 10 March 2025

Check for updates

Pengcheng Zhang[1], Yixin Zhang[1], Fei Wu[1] ✉, Weixiang Xiao[1], Weiwei Hua[1], Ziwen Tang[1], Wei Liu[1], Suwen Chen[1], Yaxing Wang[2] ✉, Wangsuo Wu[1] & Duoqiang Pan[1] ✉

Selective extracting uranium from seawater is quite challenging, particularly the presence of vanadium, which poses a significant obstacle for most amidoxime absorbents. Adsorbents with size-matched pores and coordination environment can improve the uranium selectivity but usually deteriorate the adsorption capacity. Herein, a dynamically matched spatial coordination strategy is proposed to improve the performance of uranium extraction. The diarylethene (DAE) photoswitch with photoisomerization characteristic is introduced into Metal-Organic Frameworks (MOFs), in which the tunable pore size and coordination environment provide a precisely confined space for uranium capture under the dynamic adjustment of ultraviolet-visible (UV-Vis) irradiation. Proposed material with photo-responsive gated rectification capability can effectively extract uranium from vanadium-rich system, the uranium adsorption capacity reaches 588.24 $mg \cdot g^{-1}$ and the U(VI)/V(V) separation factor ratio is recorded up to 215. Finite element simulation confirms the enhancement of mass transfer under the open-state of DAE, which leads to the improved adsorption capacity. Density Functional Theory (DFT) calculations suggest size-matching between pore structure and uranium species, as well as the spatial coordination between the closed-state DAE and uranium species, results in the U(VI)/V(V) selectivity and uranium extraction performance. Current work presents a promising strategy for improving the uranium extraction ability and U(VI)/V(V) selectivity under seawater environment.

Uranium is a crucial and safeguarded resource required for nuclear energy development[1]. The oceans contain about 4.5 billion tons of uranium, nearly a thousand times more than on land[2]. The selective extraction of uranium from seawater is promising but still challenged by the extreme low uranium concentration (3.3 ppb) as well as a large number of interfering ions[3]. For the currently well accepted adsorption approach, the well-designed bonding structures are critical in governing the selectivity towards uranium, in which the amidoxime functioned adsorbents with high adsorption capacity and selective bonding ability have drawn numerous attentions[4]. However, such materials show limited selectivity for uranium and vanadium, the separation factors (SF) were usually less than 5 dues to the formation of cyclic imide-dioxime structure between excessive adjacent amidoxime groups[5,6].

[1]Frontiers Science Center for Rare Isotopes, School of Nuclear Science and Technology, Lanzhou University, Lanzhou, China. [2]State Key Laboratory of Radiation Medicine and Protection, School of Radiation Medicine and Protection, Collaborative Innovation Center of Radiological Medicine of Jiangsu Higher Education Institutions, Soochow University, Suzhou, China. ✉e-mail: wuf@lzu.edu.cn; yxwang@suda.edu.cn; panduoqiang@lzu.edu.cn

The significant geometric configuration difference between the prevailed uranium species $[UO_2(CO_3)_3]^{4-}$ and vanadium species $[H_2VO_4]^-$ inspires researches to improve the selectivity by constructing an accurately size-matched pore structure[7,8]. Benefiting from the modifiable internal pore structure and abundant active sites, the metal organic frameworks (MOFs) could provide a large amount of locally confined geometrical space for the spatial coordination with guest ions[9–11], making it a potential candidate for the selective separation. In general, the size-matched pores are supposed to improve the uranium selectivity through a size-sieving effect[12]. For instance, the porous UiO-66-3C4N and DUT-5-POR materials containing uranyl compatible pores were proposed and have improved the $SF_{U/V}$ to 17.03 and 25.66, respectively[13]. However, the precisely matched pore will remarkably reduce the mass transfer ability and the accessibility of binding sites for target ions, which will suppress the advantage of the abundant active sites and lead to a relative low adsorption capacity, the adsorption capacity of UiO-66-3C4N and DUT-5-POR materials are merely 393.97 $mg{\cdot}g^{-1}$ and 263.4 $mg{\cdot}g^{-1}$, respectively[14]. The appropriate enlargement of pore size will increase the adsorption capacity by optimizing the mass transfer process, but this is still not a feasible solution for balancing the selectivity and capacity, as it will deteriorate the selectivity by decreasing the coordination stability of target ions in the interior pore[15]. Therefore, an effective solution to such dilemma should be developed.

The dynamically regulated MOFs with tunable pore structures have been proposed for efficient separation of mixtures with different sizes, which offered some hints for solving the dilemma[16,17]. The reversible expansion and contraction of pores in MOFs (known as breathing behavior) triggered by the feasible modulation of external light enabled the inspiring separation efficiency for the similar guest molecules[18–20]. For instance, with the light-preferred structure modulation and the guest discriminatory deriving from gate effect, a framework with photoisomerization capability enabled an efficient C_2H_2/C_2H_4 separation (SF = 47.1) at 195 K and 100 kPa with the help of UV modulation[21]. The diarylethene (DAE) offers unique structural characteristics for the photo responsible modulation, in which the reversible bond deriving electron rearrangement between two amenable rings under different irradiation leads to the cis-trans isomerization (regarded as the open and close states, respectively)[22–27]. In addition, the presence of a heteroatom with a lone pair of electrons in DAE makes potential coordination interactions with guest molecules possible[28,29]. Therefore, the DAE derivatives are promising ligands that could be integrated into the framework to induce the structural modulation for efficient separation of U(VI) from V(V) species.

Herein, we propose a viable dynamic light-responsible size-match coordination strategy in this work to achieve the highly selective capture of uranium, in which a light-responsible pore structure with dynamic size-modulating ability and spatial coordination ability offers a favorable coordination environment for target uranium species. In the opened state modulated by the visible light, the flexible pore structure facilitates the movement of ions through the pore and increases the accessibility of target $[UO_2(CO_3)_3]^{4-}$ to binding sites, which will lead to high adsorption capacity. When the pore structure of MOFs was modulated by UV light as the closed state, the relatively rigid and shrink structure provides not only the precisely size matched pore for $[UO_2(CO_3)_3]^{4-}$, but also effective coordination environment for $[UO_2(CO_3)_3]^{4-}$ rather than $[H_2VO_4]^-$. Both two features will be beneficial for selective extraction of U(VI) over V(V). To the best of our knowledge, such strategy was never reported in the field of uranium extraction from seawater but were proved to be very effective in this paper, as high uranium extraction ability (588.24 $mg{\cdot}g^{-1}$) and unprecedented U(VI)/V(V) separation factor (215) were achieved.

Specifically, in this work, a light responsible framework material was manufactured by integrating the photosensitive DAE isomerization into two stable zeolite imidazolate frameworks (ZIFs) with similar chemical composition but different pore size, ZIF-70 and ZIF-60, respectively[30]. The ionic rectification regulation inside the pore structure under the bistable state of DAE isomerization was evaluated by employing the finite element simulation. The photochemical behavior, photoswitch-fatigue resistance, adsorption capacity and adsorption selectivity were investigated under the above two states. In addition, the adsorption performance of the proposed photoisomeric materials was examined in natural seawater systems with high salinity and high concentrations of competing ions. The proposed composites exhibited impressive U(VI)/V(V) selectivity and adsorption capabilities while maintaining the structural stability for long periods. The mechanism for the precise identification and selective capture of uranium were also analyzed in depth with the aid of theoretical calculations.

Results and Discussion

MOFs structural characterization

The structure of photoswitch grafted frameworks, the photoisomerized process, and the spatially confined coordination of proposed materials were depicted in Fig. 1. Figure 2a, b and Supplementary Figs. 2–5 show the morphologies of ZIF-70 and ZIF-60 before and after photoswitch loading, respectively. The macroscopic prismatic structures of the two materials did not exhibit obvious changes after long-term heat treatment with organic solvents due to the excellent thermal stability of the materials[31,32]; however, a certain number of lamellar intercalation structures appeared on the surfaces of the materials. These structures were consistent with the morphology of the HL1 (4,5-bis(2,5-dimethyl-3-thienyl)-1H-imidazole) photoswitch monoliths that formed via self-assembly (Supplementary Fig. 1) and were successfully integrated into the materials. In addition, elemental mapping analysis revealed that the sulfur present in the thiophene functional groups of HL1 photoswitches was uniformly distributed on the surfaces of the two materials (Fig. 2c, d), and there was a strong correlation between the distribution trend and the zinc atoms serving as metal nodes, which suggested that stable bonding occurred between the structural elements that composed the MOFs materials, which is also one of the elements in constructing the coordination microenvironment within the framework. Comparing the changes in the integral areas of the characteristic peaks in the ^{1}H NMR (^{1}H Nuclear Magnetic Resonance) spectra of the composite photoisomeric MOFs materials (Photoswitch-ZIFs, i.e. PSZ-60 and PSZ-70) (Supplementary Figs. 6–10), we determined that the grafting rates of the photoswitches reached 18.32% (PSZ-70) and 10.41% (PSZ-60). As a functional unit in the material, although HL1 exhibits its photochemical behavior, the coordinating process of sulfur atoms to uranium in the molecule cannot be ignored as well. More importantly, for PSZ-70 and PSZ-60, the proportion of sulfur present will directly affect the performance of the two materials in terms of uranium adsorption capacity[33–35]. Considering the differences in the crystal configurations, it was concluded that this discrepancy mainly derived from the difference in the size of the window diameter (d_a) and aperture diameter (d_p), leading to exchange failure at some of the nonequivalent imidazole junctions during the solvent-assisted ligand exchange (SALE) process. For considering the thermal stability of the grafting process between the two materials, we tested the grafting rate of HL1 inside the two materials at different time points of the current heat exchange temperature, as shown in Supplementary Fig. 11. It is evident that the grafting rate does not significantly improve with the ligand exchange time after 4 days, but rather has a weak adverse effect on the thermal stability of the materials themselves. The XRD (X-ray Diffraction) patterns of these two MOFs materials and their corresponding modified photoisomers are shown in Supplementary Fig. 12. Zeolite imidazole ester, a typical hydrophobic structure, has a considerable degree of spatial resistance[36,37]. Therefore, the two thiophene rings of HL1 added steric effects to the imidazole group coupled with the metal node, resulting in the crystallinity of PSZ-70, as shown in the figure, being better than

https://doi.org/10.1038/s41467-025-57638-4

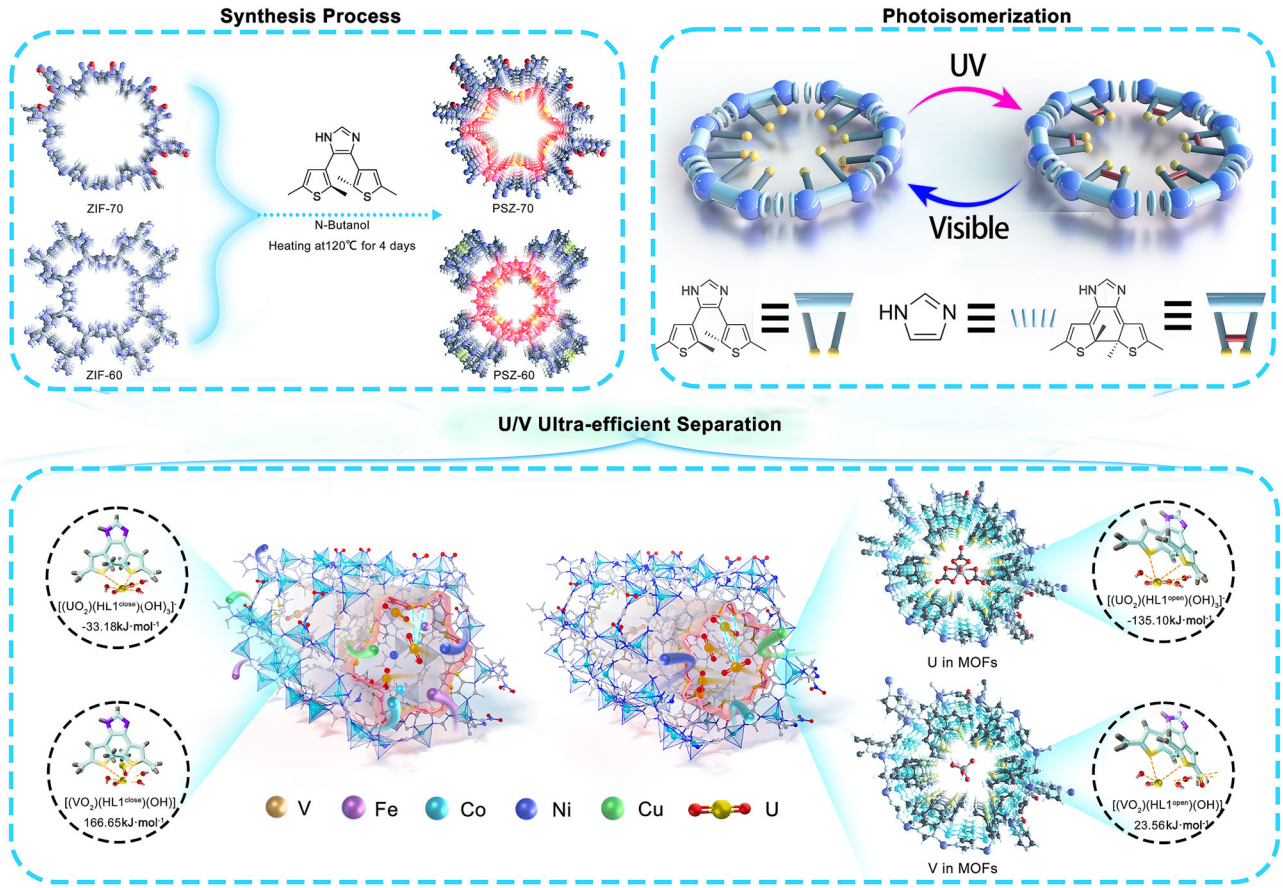

Fig. 1 | Construction of a composite photoisomeric material framework and illustration of the selective uranium extraction process. Synthesis Process Section Grafting of photoisomerization monomers in ZIF-60 and ZIF-70. Photoisomerization Section Photo-responsive isomerization of composite photoisomerized MOFs. U/V Ultra-efficient Separation Section Differential recognition and separation of U(VI) and V(V) by composite photoisomerized MOFs in a polymetallic ion interference system.

that of ZIF-70[38]. ZIF-60 (d_a=7.2 Å), with half size of ZIF-70 (d_a=13.1 Å), possesses greater steric hindrance and thus results in a partial decrease in the intensity of lower-angle peaks and an increase in the relative intensity of higher-angle peaks. This subtle change was also consistent with the grafting rate results reflected in the previous ^{1}H NMR spectra.

Before pursuing any further investigation, we obtained a theoretical infrared spectrum (Supplementary Fig. 13) by modeling and optimizing the chemical structure of the photoisomeric unit HL1 using Gaussian 16 software. The experimental spectrum of the synthesized product displayed absorption peaks at 1140, 1210, 1260, and 1300 cm^{-1} (red area in Supplementary Fig. 14), which are consistent with the theoretical values and verify the designed photoswitch's distinctive chemical structure of the product. Furthermore, we performed N_2 (77 K) gas adsorption tests on the MOFs materials before and after HL1 photoswitch grafting, and the corresponding results are shown in Supplementary Fig. 15. With larger specific surface area, ZIF-70 possesses more intrinsic active sites than ZIF-60[39]. As determined from the reduction in the specific surface area of the two substrate MOFs after grafting the photoswitch, the size of the photoisomerization unit introduced basing on the same ligand exchange indirectly reflects the advantage of ZIF-70 over ZIF-60 in terms of the pore size and the effective number of structural pores, which was also reflected in the relevant characterization results mentioned above.

Photochemical behavior studies

Molecular orbitals for a few DAEs with a structure comparable to that of HL1 were obtained through Density Functional Theory (DFT) simulations using Gaussian 16 package (Fig. 2e). The energy difference between the highest occupied molecular orbital (HOMO) and the lowest unoccupied molecular orbital (LUMO) determines the optical range of a molecule[40]. According to the quantum theory of molecular photochemistry, an extended π-conjugation system increases the number of coupled molecular orbitals and enhances the degree of π-dissociation, and the methyl group at the side chain end of the thiophene ring can further extend the optical absorption band of DAE molecules through its electron-donating effect to enhance the efficiency of cyclization switching[22]. Therefore, we used ultraviolet-visible (UV-Vis) spectroscopy to evaluate the optical characteristics of the HL1 photoswitchable monomer dissolved in methanol (Fig. 2f). The spectrum of HL1 displayed varying degrees of absorption at 285, 340 nm, and 545 nm within 10 min, during which time the color of the solution gradually changed from purple to crimson, which was assumed to indicate a change from the open-loop conformation to the closed-loop conformation upon irradiation with UV light (λ = 253.7 nm)[41]. In addition, the red color soon faded to an almost undetectable light yellow when the irradiation source was changed to visible light at a wavelength of 515 nm (Supplementary Fig. 16)[42]. The increase and decrease in the absorption bands at 535-550 nm in the spectra of the DAE series derivatives were attributed to the corresponding photoisomerization cycle process[43]. Therefore, based on the above results, we monitored the changes in absorbance at 545 nm with time and observed a clear fluctuation trend corresponding to a single open-closed conformational transition of the HL1 photoswitch molecule. To further explore whether the HL1 molecule can maintain its closed state for a long time, the change in absorbance of

https://doi.org/10.1038/s41467-025-57638-4

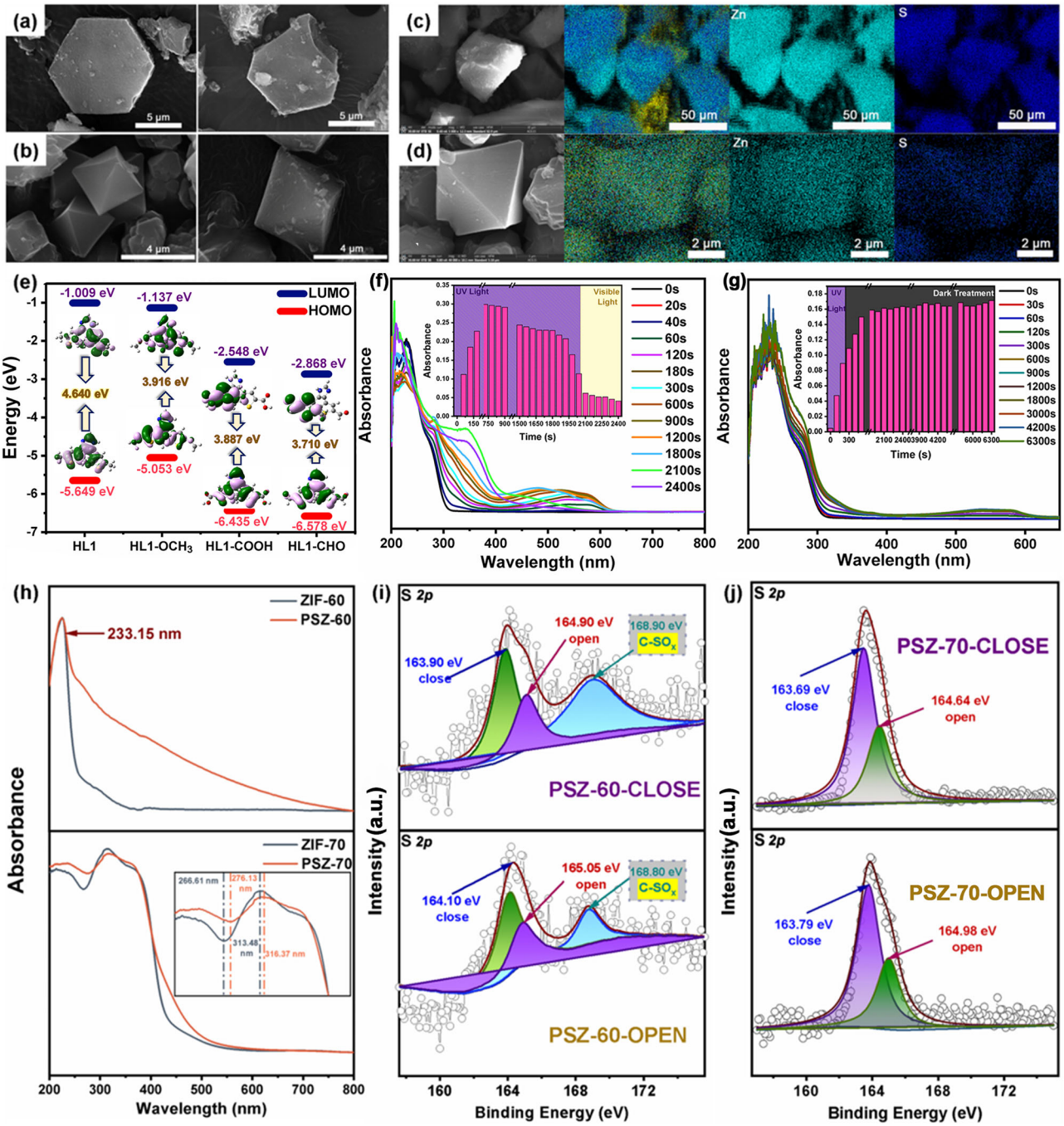

Fig. 2 | Characterization of physical and chemical properties of materials. a SEM images of ZIF-70 (left) and PSZ-70 (right). **b** ZIF-60 (left) and PSZ-60 (right). **c**, **d** SEM images and EDX analysis (C(yellow), N(green), O(red), Zn(turquoise), S(dark blue), subgraphs from left to right are the composition of all elements, Zn and S, respectively) of PSZ-70 (up) and PSZ-60 (down). **e** Molecular orbital diagram of HL1 and corresponding partial derivatives. **f**, **g** Absorbance of HL1 in a methanol solution in the wavelength range of λ = 200–800 nm under UV–visible switching light source conditions (left) and UV-dark conditions (right) (the inset figures in both 2f and 2g show the absorbance change of the solution anchored at 545 nm, respectively). **h** DRS analysis of ZIF-70, ZIF-60, PSZ-70, and PSZ-60 (The top and bottom graphs show the change of absorbance in the range of 200–800 nm before and after grafting the photoswitch with ZIF-60 and ZIF-70, respectively; the inset figure of bottom graph is an enlarged display of the spectrum in the range of 200–400 nm). **i** XPS analysis of the open/closed conformational transition process of PSZ-60 (The top and bottom graphs show the binding energy changes of the splitting peaks in the S *2p* spectra of PSZ-60 in the photoisomerized open-state and closed-state). **j** XPS analysis of the open/closed conformational transition process of PSZ-70 (The top and bottom graphs show the binding energy changes of the splitting peaks in the S *2p* spectra of PSZ-70 in the photoisomerized open-state and closed-state).

HL1 at 545 nm in the dark after removing the light source after 10 min of UV irradiation were investigated (Fig. 2g). As expected, the change in absorbance during the first 10 min of UV exposure gradually increased, suggesting that the proportion of the closed structure in the mixed system increased steadily during this time. After a long period in the dark, the absorbance at 545 nm did not change significantly. Therefore, artificial adjustments in the irradiation time can precisely control the photoswitching process of DAE molecules to achieve the appropriate closed state and maintain this state for a long time without interference from outside light sources.

The light absorption patterns of the two substrates and the corresponding photoswitchable modification products were analyzed in the wavelength range of 200–800 nm using diffuse reflectance spectroscopy (DRS) (Fig. 2h). The grafting of the HL1 monomer significantly increased the absorption in the range of 233–800 nm for ZIF-60, which had almost no absorption in the visible region. Therefore, the ability of composite materials to modulate light absorption was almost entirely due to the photoswitching of molecules with broad photochemical responses[44]. Owing to the higher grafting ratio, such a change was also observed in the ZIF-70 and PSZ-70. Notably, the strong UV-absorbing properties of the ZIFs series of materials were not affected despite the long ligand exchange process occurring in a high-temperature organic solution atmosphere[45]. In addition to this, the DRS spectra of PSZ-70 absorbance versus time under the same UV irradiation conditions similarly exhibited a rise and fall change consistent with that of the monomer (Supplementary Fig. 17), indicating that the SALE process did not detract from the photoswitching activity. This retention of substrate dominance suggested the potential for synergistic isomerization conversions by considering the previous fast-closed cyclization kinetics upon UV irradiation of HL1 monomers.

Based on the analysis of the S *2p* spectra in the X-ray photoelectron spectroscopy (XPS) of PSZ-70, the S $2p_{3/2}$ peak with a binding energy of 163.79 eV is usually considered to indicate a closed structure between the thiophene rings, whereas the other set of S $2p_{3/2}$ component peaks located at 164.98 eV corresponds to the open form (Fig. 2i)[46]. Based on the unique chemical structure of the DAE molecule, it is not difficult to understand the difference between the binding energy in the two isomeric states, i.e., the underlying reason comes from the presence or absence of aromaticity in both states[47]. In the photoswitch-closed state, DAE loses its intrinsic aromaticity, thus favoring a more extensive conjugation of electrons throughout the molecule, and this rearrangement also determines the final position and peak shape of the split peak signal. Anomalously, however, in the spectrum of PSZ-60, in addition to the two similar splitting peaks appearing therein compared to PSZ-70, a new S $2p_{3/2}$ splitting peak with a binding energy close to 169 eV appears (Fig. 2j). It is generally believed that broader peaks such as the above peaks centered at 168-169 eV are attributed to the formation or transformation of oxidation products of elemental sulfur, and more specifically to the generation of isolated sulfur atoms or thiols due to the irradiation of X-rays[48,49]. In contrast to DAE molecules loaded in ZIFs substrate materials with different pore sizes, the reason is related to the possibility with which the C-S-C bonds in thiophene are broken under the same test conditions. The stability of the MOFs themselves, as components integrated into the material framework in the form of identical linker substitutions, influences the strength of the ligand bonds therein[50]. As for the only different components in the two substrate materials, 2-nitroimidazole and 2-methylimidazole, the nitro group with a strong electron-attracted effect contained in 2-nitroimidazole can effectively reduce the excessive electron density in the system after grafting DAE, thus providing stronger stability for the framework[51]. On the contrary, the methyl group with an electron-donating effect increases the repulsive force between electrons, making the chemical bonds in the framework more susceptive for bond breakage[52], and the increase in the area of the sulfur oxide splitting peak for the closed state is also strong evidence for this analysis.

Ion rectification behavior in COMSOL multiphysics field simulations

The gating rectification ability of the photoisomerization composites was investigated through developing a theoretical model using COMSOL Multiphysics 6.0 software. Figure 3a depicts the differential changes inside the pore channel of two photoisomerized composite MOFs materials in the isomerization bistable state, which mainly serves to introduce this conformational difference to visualize the model construction, the geometrical structures in the on and off states that were modeled in Fig. 3b. Additionally, the Poisson–Nernst–Planck equation was applied to solve the problem of ion transport in electrostatic and dilute matter transfer fields at physical field interfaces. Time-independent flux expressions were established since all the processes involved were steady-state processes. The relevant boundary conditions and parameter settings are summarized in the Supplementary Information (Supplementary Table 1 and 2)[53].

Figure 3c, d depict the behavior of electrolyte solution ions migrating inside the pore channel of the photoisomerization material as driven by an electric field. The ion rectification behavior of the nanopore channels was investigated at pH=2 and pH=8 (Supplementary Figs. 18,19), and the charge density of the DAE surface was configured as positive for acidic conditions and negative for alkaline conditions. Notably, there was a significant correlation between the electrical characteristics of the charge density on the surface of the nanopore channel and the positive and negative applied external electric fields for various acidic and alkaline solution environments. When the two electrical properties were equivalent, the ion flux inside the pore was lower than that in an electrolytic cell simulation, and when the opposite was true, the ion enrichment inside the pore was greater, a phenomenon that can be as attributed to electrostatic action. Ions with the opposite electric field were enriched in the inner wall of the pore under alkaline conditions; for instance, according to diffusive double layer theory, ions with the same electric field were distributed diffusely inside the pore, generating an additional electrostatic field force with increasing local charge density, which increased the swimming motility. The buildup of the ion flow was observed to increase. The migratory behavior of ions within nanopore channels, on the other hand, was primarily driven by changes in surface charge when the pore surface charge density was opposite to the external electric field. The number of ions with opposite electrical characteristics increased with the surface charge density of the nanopore channel, and the thickness of the adsorbed layer increased equally. The interfacial tension decreased as the repulsive force between homogenous charges increased. This, in turn, increased the corresponding free-ion flow and resulted in a comparatively low accumulation on the inner wall of the pore channel.

Supplementary Fig. 20 shows the ion flux fluctuations of the photoisomerized material in the open and closed states, respectively. When the two migration modes had the same voltage and surface charge density, there was little difference between them in general, but there was a significant difference in behavior at the predefined solid–liquid interface junction and inside the composite pore channel. Figure 3b shows that the subjective adjustment of the closure structure of the photoswitch geometry model resulted in a relative reduction in the channel pore size (yellow). In addition, the pore structure of the longitudinally asymmetric influenced the tendency of the absolute value of the ion current to vary with the potential gradient[54]. The diffuse bilayer produced in this case was closer to or even wider than the pore size of the adsorbed layer and exhibited a more pronounced ion rectification capacity than the photoswitch open state. Therefore, the introduction of DAE photoswitches allowed fine-tuning of the pore channels that ions migrate through, which was indicative of gated rectification ability.

Uranium adsorption behavior

Adsorption tests were conducted based on a simulated seawater system (Supplementary Fig. 21)[55]. Before conducting detailed adsorption studies, the stability of two substrate materials across a range of solution acidity and alkalinity were assessed (Supplementary Fig. 22). The dissolution percentage of Zn(II) revealed the intolerance of MOFs materials with imidazolium-based backbones to such conditions. On the other hand, the exceptional stability exhibited by both materials in weakly basic to basic environments serves as the foundation and

https://doi.org/10.1038/s41467-025-57638-4

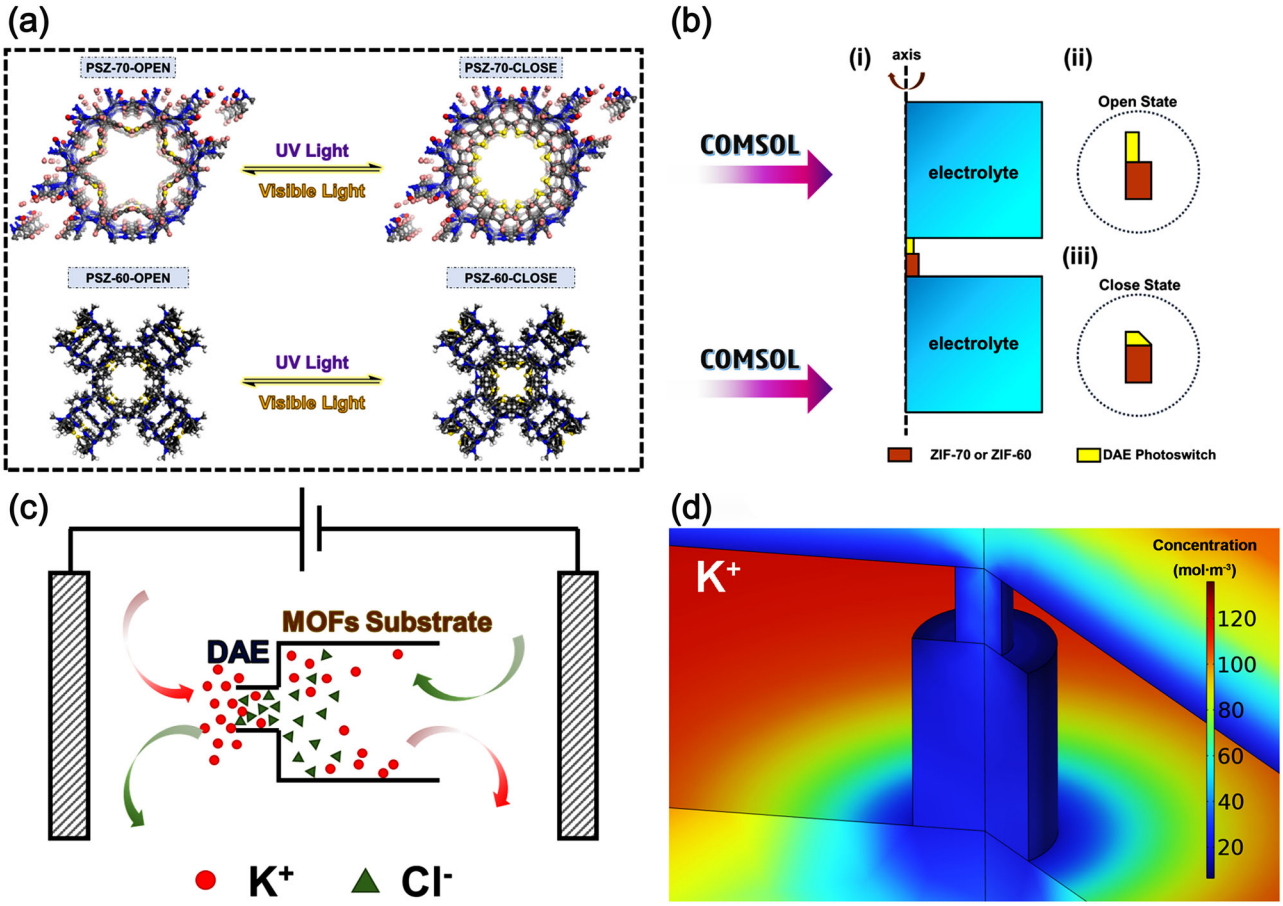

Fig. 3 | Finite element modeling and mass transfer simulation of the photoisomerized MOFs. a Diagram of the theoretical open/closed conformational transition of PSZ-70 and PSZ-60. **b** Simulation of the structure of the composite material in COMSOL software in the open and closed states of the photoswitch ((i) Construction of axisymmetric model; (ii) the two-dimensional geometric model of the pore structure when the photoswitch is under the open-state; (iii) the two-dimensional geometric model of the pore structure when the photoswitch is under the closed-state). **c** Illustration of the swimming behavior of ions in photoisomeric composites driven by an electric field (with K^+ and Cl^- as examples). **d** Heatmap of the concentration flux of K^+ in the experimentally simulated system in the photoswitch open state.

crucial prerequisite for investigating the adsorption and separation behavior of the materials in subsequent studies. As shown in Fig. 4a, when the pH increased from 3 to 5, the adsorption capacity of the material increased significantly. On the one hand, this increase was mainly due to the increase in the content ratio of the positively charged multinuclear hydroxide species of uranium, such as UO_2^{2+}, $[UO_2(OH)]^+$, $[(UO_2)_2(OH)_2]^{2+}$ and $[(UO_2)_3(OH)]^{5+}$, which reduced the net charge content between the adsorbent and the adsorbate and thus resulted in the weakening of the repulsion effect. On the other hand, the chelating coordination ability between uranium and the protonated imidazole group in the molecular skeleton of the material was enhanced, which improved the adsorption capacity[56]. When the solution system was in a weakly alkaline environment at pH=7 ~ 10, the surface charge of the above material was negative, and the proportion of negatively charged uranium species was similar to that of $[UO_2(CO_3)_3]^{4-}$, $[UO_2(OH)_3]^-$ and $[(UO_2)_3(OH)_7]^-$. Additionally, the proportion of these species increased with increasing pH, thus leading to an increase in electrostatic repulsion during the adsorption process. The adsorption capacity significantly decreased, indicating that the binding interaction between the functional groups and the adsorbent uranium species did not dominate the course of the adsorption capacity of the material in this process.

The adsorption isotherms of ZIF-70 and ZIF-60 as substrate materials and their corresponding photoisomerized derivatives were established and fitted with the Langmuir and Freundlich models (Fig. 4b and Supplementary Table 3). The uranium adsorption capacities reached 322.58 $mg \cdot g^{-1}$ (ZIF-70) and 185.19 $mg \cdot g^{-1}$ (ZIF-60), respectively, maintaining the good adsorption ability of the MOFs series of materials[57,58]. However, with the introduction of photoswitches, the adsorption capability of PSZ-70 increased whereas the adsorption capability of PSZ-60 decreased. Without considering the influence of the grafting rate or other factors on the adsorbent itself, the key to determining the difference in the adsorption capacity is the flux of the adsorbate in different pores. To verify this conjecture, we adjusted the substrate in equal proportion to the difference in pore sizes between ZIF-70 and ZIF-60 based on previous simulations and examined the transferring behavior of ions induced by electric fields in subsections (Fig. 4c). Using the previously established two-dimensional intercept line inside the aperture as a reference system, it was found that the ion flux decreased sharply with increasing distance inside the PSZ-60 compared to that inside the PSZ-70. Extending this phenomenon to the actual adsorption process indicated that the introduction of the HL1 photoswitch instead hindered the entry of the uranium species into the interior of the ZIF-60 pore, which was visualized as a decrease in the adsorption capacity of the material.

As shown in Fig. 4d and Supplementary Fig. 23, under the same UV irradiation conditions, the maximum adsorption capacity of the two photoisomerized composites varied with respect to the irradiation time. The imidazole unit of the HL1 monomer in the open-loop state included six π electrons, a nonaromatic Schiff base was formed when

https://doi.org/10.1038/s41467-025-57638-4

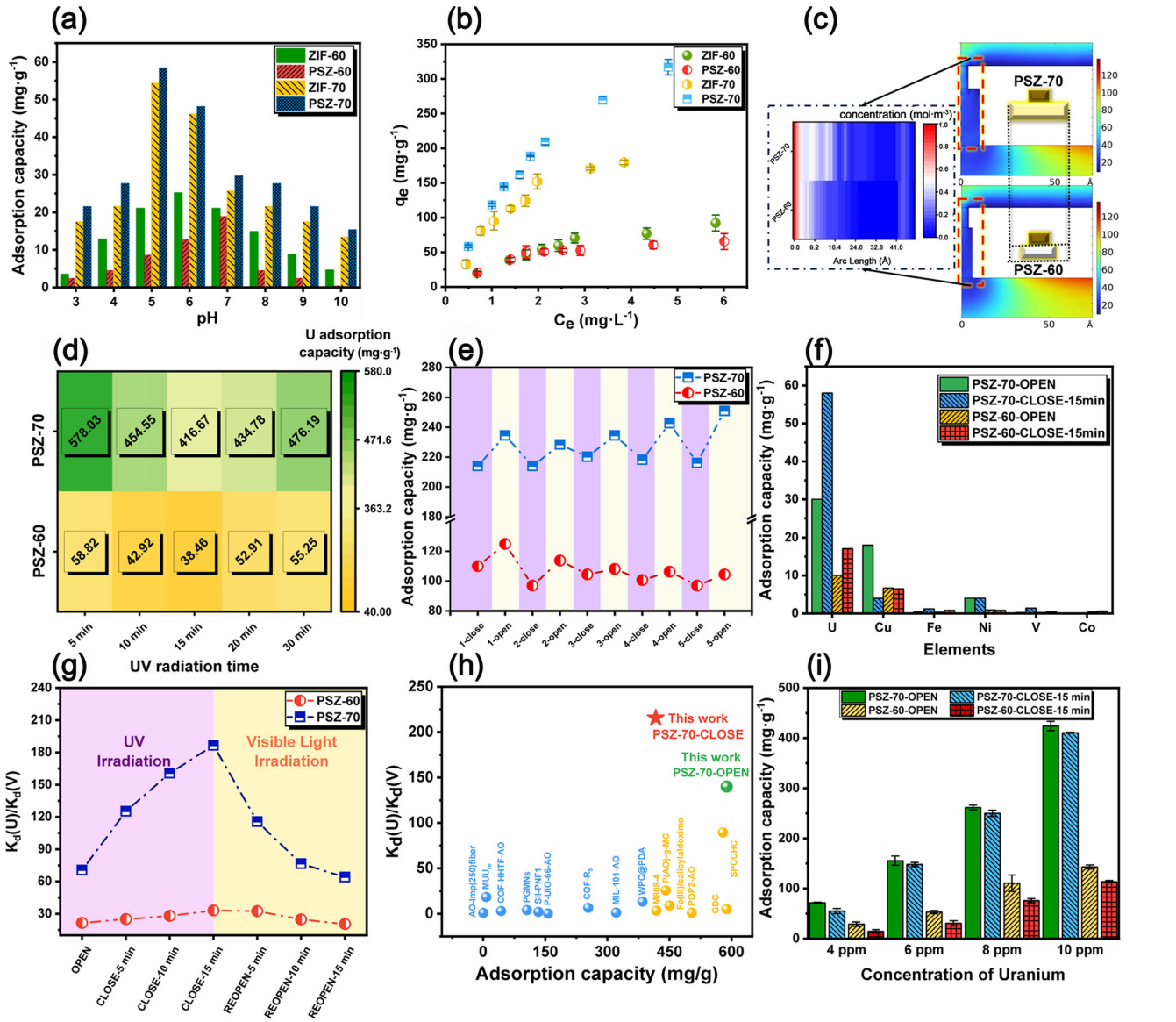

Fig. 4 | Adsorption and separation of uranium by the composite photoisomerized MOFs. a Variation in the maximum adsorption capacity with pH for ZIF-70, PSZ-70, ZIF-60, and PSZ-60. **b** Adsorption isotherms of two substrate MOFs and their corresponding photoisomeric composites at 298 K. **c** Visualization of ion swimming by different substrate pore sizes of MOFs. **d** Comparison of the maximum adsorption capacity of uranium by the photoisomerization process of PSZ-70 and PSZ-60. **e** Photoisomerization fatigue test under alternate UV-Vis exposure cycles (Purple color indicates the absorbance measurements under UV irradiation, yellow color indicates the absorbance measurements under visible light irradiation, and the bar widths do not correlate with the measurement duration. Number-close indicates the number of times the photoswitch was in the closed state during the five cycles test (i.e., the photoswitch was in the closed state for the nth time ($n = 1, 2, 3, 4, 5$)), and this description also applies to the open state). **f** Adsorption selectivity of PSZ-70 and PSZ-60 with their corresponding open/closed isomeric states for some metal cations in simulated seawater systems. **g** Test of the separability of uranium and vanadium by in situ photocontrolled reversible isomerization. **h** Comparison of the maximum adsorption capacities and U(VI)/V(V) separation ratios of photoisomerized MOFs with adsorbent materials in some of the similar experimental systems. **i** PSZ-70 and PSZ-60's adsorption abilities in fully open and closed conformations in natural seawater with uranium spikes. Error bars in Fig. 4b and i represent standard deviations (SD) calculated from three independent replicate experiments for each data point, the SD was computed to reflect the variability of the measurements.

UV irradiation induced the closure and cyclization of its electron orbitals. Therefore, we hypothesized that the main reason for the observed phenomenon was related to the change in the photosensitive properties of the photoisomeric monomer, which explains the hysteresis in the degree of closure relative to that of the monomer shown by the change in the maximum adsorption capacity. DAE molecules with unique light-absorbing properties, the resulting change in photosensitivity was mainly the result of a change in the electron conjugation structure. Similarly, in a constrained environment such as for MOFs defined by the frame topology, the kinetic process of the cyclization reaction of the photoisomerization unit was governed by several factors, as Williams et al. concluded that the photoisomerization rate was a function of the frame topology[59].

On the premise that there is a time lag in the DAE photoisomerization process in the framework compared with that of the monomer, the changes in the adsorption capacity of the composites are deriving from the ion mass transfer and coordination processes in the pore channels. According to modeling results, with the DAE photoisomerization process, the MOFs pore size further contracted, creating unfavorable conditions for the guest adsorbate ions to enter

the framework. In addition to this, compared to the initial conformation of photoswitching, the degree of conjugation of the DAE molecules gradually increased under UV irradiation, and the electrons contained in the sulfur atoms that undergo coordination with the uranium species were averaged throughout the system, which led to the decrease in the binding capacity of DAE molecules with uranium[60–62]. Combined with the above changes in pore properties, the combined effect led to a decrease in the adsorption capacity of the composite MOFs for uranium.

It is noteworthy that with the continuous application of UV irradiation, the adsorption capacity of the two MOFs materials underwent a certain magnitude of recovery. Considering that the ring-opening reaction of DAE molecules can only be driven by visible light, the influence of the conformational transformation process involved in this process on the adsorption behavior of the materials can be excluded[63]. For adsorbent suspension systems subjected to prolonged UV irradiation, water molecules in the solvent can interact with the DAE molecules in the framework of MOFs via a hydrogen bonding network[64], thereby increasing their absorption cross-section and making them more susceptible to loss by UV radiation[65,66]. Therefore, according to the change process of the overall adsorption behavior reflected in Fig. 4d, it is not difficult to know that when the photoswitching completely reaches the closed-loop conformation, the continuous UV irradiation leads to the dissociation of part of the DAE molecules, and this ratio will further increase with the extension of the irradiation time, and a similar phenomenon is also reflected in the photoisomerization of the monomers (inset of Fig. 2f). On this basis, this leads to an increase in the effective mass-transfer region in the pore channel of the MOFs, which is displayed as a re-increase in the adsorption capacity.

Figure 4e shows the change in the adsorptive capacity of the same batch of adsorbent suspensions for the same UV radiation-induced photoswitching off and visible light-induced ring opening. In general, according to the UV-induced closed-loop mechanism of the 6π-electron system in the DAE center, irreversible photoreactions between certain homologous molecules can lead to fatigue. In response to this phenomenon, chemical methods have been widely used to expand π-conjugated systems and add electron-absorbing groups to improve the resistance of space sites, thus reducing the production of singlet oxygen in various oxidation byproducts during irradiation switching and leading to improved fatigue resistance[67,68]. In the present work, based on the perspective of slowing the aggregation of DAE molecules in aqueous solution and the resulting self-quenching phenomenon, the presence of substrate ZIFs with inherent spatial site resistance effectively protected HL1 molecules, reducing the proportion of isomerization byproducts during the above tests. Moreover, the push-pull electron effect in the liquid phase between the electron-deficient metal node and the electron-rich nitrogen end of the pyridine ring of DAE molecules effectively prevented the self-polymerization of DAE molecules, thus prolonging the photochemical lifetime and stability of the composites and providing positive feedback for maintaining the fatigue resistance of the photoswitches[69].

Selective U(VI) extraction mediated by photoisomerization process

The results of the adsorption selectivity for the composite materials are shown in Fig. 4f and Supplementary Table 4 for the two states: completely open and completely closed. The ability of both materials to selectively separate the respective isomeric states of uranium exhibited considerable variance in complex systems in which several metal ions coexist. Remarkably, the two composite MOFs showed weaker uranium adsorption ability in the open state than in the closed state. Although it may seem logical to assume that there are more active sites for adsorption in the open state than in the single uranium system, copper and other interfering ions are bound to ligands in the materials, which to some extent inhibits uranium adsorption. Additionally, Rachel et al. demonstrated that the coordination of Cu(II) to DAE derivatives following UV irradiation treatment considerably increased the amount of covalent bonding components in closed-state composite MOFs[70]. The adsorbent itself is therefore subjected to the influence of coexisting Cu(II) to enhance coordination with uranium, and the combined effect is that closed-state materials are more capable of capturing uranium in complex system. Coincidentally, based on the above discussion on the adsorption capacity of materials, from the perspective of the MOFs structure, in the closed state, the cage-like internal space carrying the guest adsorbent was isomerized, resulting in the expansion of the 6π-electron cloud of the conjugate system, which increased the accessible interact probability with the guest metal ions transferring in pore channels. Thus, the MOFs was more likely to coordinate with uranium species to form the most stable structure, which explains its excellent selective adsorption on closed-state MOFs.

Compared with a single adsorbent system, when the irradiation object is a multicomponent system, the switching kinetics of the photomodulated conformation of the material at different times are completely unknown. Considering the influence of the adsorption process, the open-closed loop switching within the HL1 monomer molecule necessarily occurs in coordination with the uranium-vanadium species. The monotonic variation in the U(VI)/V(V) separation factor upon irradiation with different light sources and the higher separation capacity demonstrated in previous selectivity tests, while reflecting the adverse effect of material adsorption on photoisomerization, also confirmed the occurrence of photodesorption at a certain level (Fig. 4g).

Figure 4h shows the U(VI)/V(V) separation factor of the as-constructed photoisomeric composites in both states and compares them with the reported uranium extraction results under the corresponding conditions (Supplementary Table 5 lists the relevant conditions and data)[71–83]. Considering the variability of the experimental systems, the U(VI)/V(V) separation factor of the as-constructed photomodulate isomerization material were the highest recorded to date for applications in simulated seawater systems due to the synergic effect between coordination process and special geometrical constraints, demonstrating the effectiveness of the strategy of selective uranium separation by using photoswitching units. The capacity for extraction in natural seawater with spiked uranium was investigated to further evaluate the feasibility and application of the technique of uranium adsorption by photoisomeric materials in complicated marine settings (Fig. 4i)[84]. The maximum adsorption capacities of the two photoisomeric composites increased as the concentration of the adsorbent substrate increased in both the completely open and completely closed states, demonstrating the strong affinity of these materials for uranium in the natural environment. Therefore, it is reasonable to conclude that MOFs loaded with HL1 molecular photoswitches can meet the demand for uranium extraction under real seawater site conditions and further contribute to the goal of high-efficiency and low-cost uranium enrichment due to the unique feature of light-modulated isomerization.

DFT calculations of the adsorption configuration

To provide a comprehensive understanding of the coordination structure and metal-ligand bonding, as well as to explain the reasons behind the higher uranium adsorption capacity of PSZ-70 (588.24 $mg{\cdot}g^{-1}$) compared to ZIF-70 (322.58 $mg{\cdot}g^{-1}$), the higher U adsorption capacity of the open states of PSZ-70/PSZ-60 (588.24/84.75 $mg{\cdot}g^{-1}$) compared to the close states (416.67/38.46 $mg{\cdot}g^{-1}$), the achievement of a high U(VI)/V(V) SF for PSZ-70/PSZ-60, and the higher U(VI)/V(V) SF of the close state (215.28/33.45) compared to the open state (139.8/27.77), we conducted DFT simulations of complexes formed from HL1 and UO_2^{2+} (or VO_2^{+}). It is worth noting that, based on

the analysis of the change in adsorption capacity of ZIF-60/PSZ-60 in Fig. 4b, c due to its internally limited mass transfer capacity, there is a limitation in using DFT to account for the HL1 coordination capacity of this material alone. At this time the numerical relationship reflected in ΔG is only used to evaluate the binding capacity of HL1 to U(VI)/V(V). Several possible complexes (Supplementary Figs. 24–27), each with different numbers of HL1, H_2O, Cl^-, SO_4^{2-}, OH^-, CO_3^{2-}, and UO_2^{2+} (or VO_2^+) units were simulated, and the complex with the lowest U(VI)/V(V)-ligand binding energy (ΔG) was identified as the most stable complex (Fig. 5a–k). Although Cl^- and SO_4^{2-} are most abundant anions in seawater, their complexes with HL1 and UO_2^{2+}/VO_2^- shows significantly higher binding energies (more than 200 kJ·mol^{-1} higher in ΔG). With significantly smaller energy barriers, the UO_2^{2+}/VO_2^- and HL1 tend to form complexes with OH^- instead of Cl^- and SO_4^{2-}. Therefore, from energetic perspective, the impact of Cl^- and SO_4^{2-} on the U extraction ability of our MOFs could be relatively small.

As can be seen, from Fig. 5a, b, both the closed and open states of HL1 coordinated to UO_2^{2+} via 3 hydroxyl groups, forming a $[(UO_2)(HL1)(OH)_3]^-$ complex. Since uranium mainly exists in the form of $[UO_2(CO_3)_3]^{4-}$ in seawater[85], the complexation reaction can occur as follows:

$$[UO_2(CO_3)_3]^{4-} + HL1 + 3OH^- \rightarrow [UO_2(HL1)(OH)_3]^- + 3CO_3^{2-}$$

Further analysis suggested that seven metal-ligand bonds (Fig. 5e–k) were present in the $[(UO_2)(HL1)(OH)_3]^-$ complex, with three double bonds between U and the O of OH^- groups and a single bond between U and the S in the HL1 moiety. The composition of each bond is described in Supplementary Table 6. The seven bonds stabilized the $[(UO_2)(HL1)(OH)_3]^-$ complex, making the complexation reaction exothermic. Specifically, the ΔG values of $[(UO_2)(HL1^{open})(OH)_3]^-$ and $[(UO_2)(HL1^{close})(OH)_3]^-$ were −135.10 kJ·mol^{-1} and −33.18 kJ·mol^{-1}, respectively. Previous research based on three reactions of uranyl complexes with glutarimidedioximate ligands suggested that the ΔG value determined from these DFT simulations is reliable for predicting the trends of the reactions[86]. Therefore, the low ΔG explained why PSZ-70 had a greater uranium adsorption capacity than ZIF-70.

Although the same type of bonding and identical chemical composition were observed for $[(UO_2)(HL1^{open})(OH)_3]^-$ and $[(UO_2)(HL1^{close})(OH)_3]^-$, differences in the coordination structure were still observed. In $[(UO_2)(HL1^{open})(OH)_3]^-$, the dimethylthiophene unit that was not directly coordinated with UO_2^{2+} rotated to reduce the steric hindrance between UO_2^{2+} and this group, which was impossible in $[(UO_2)(HL1^{close})(OH)_3]^-$ since the two dimethylthiophene groups were linked together in $HL1^{close}$. Consequently, in $[(UO_2)(HL1^{open})(OH)_3]^-$, UO_2^{2+} remained closer to the S atoms, forming stronger U–S bonds and making $[(UO_2)(HL1^{open})(OH)_3]^-$ more stable than $[(UO_2)(HL1^{close})(OH)_3]^-$. Specifically, the U-S distance in $[(UO_2)(HL1^{open})(OH)_3]^-$ is 3.24 Å, which is 0.09 Å shorter than the distance in $[(UO_2)(HL1^{close})(OH)_3]^-$ (3.33 Å). Consequently, the ΔG of $[(UO_2)(HL1^{open})(OH)_3]^-$ was 101.92 kJ·mol^{-1} lower than the ΔG of $[(UO_2)(HL1^{close})(OH)_3]^-$, which could explain why the U adsorption capacity of the open state of PSZ-70/PSZ-60 was greater than that of the closed state.

Figure 5c, d suggest that both the closed and open states of HL1 coordinate to VO_2^+ via one OH^-, forming a $[(VO_2)(HL1)(OH)]$ complex. Since the literature implies that vanadium mainly exists as $[H_2VO_4]^-$ in seawater[87], the complexation reaction can occur as follows:

$$[VO_2(OH)_2]^- + HL1 \rightarrow [VO_2(HL1)(OH)] + OH^-$$

In the $[(VO_2)(HL1)(OH)]$ complex, only two metal-ligand bonds (Supplementary Fig. 29) were observed, including a single bond between V and the O atom of the OH^- group and a single bond between V and the S atom in the HL1 moiety. The composition of each bond is described in Supplementary Table 7. With fewer bonds available to stabilize the complex, the complexation reaction became endothermic, and the ΔG values of $[(VO_2)(HL1)(OH)]$ were significantly greater than those of $[(UO_2)(HL1)(OH)_3]^-$. Specifically, the ΔG of $[(UO_2)(HL1^{open})(OH)_3]^-$ was 158.66 kJ·mol^{-1} lower than that of $[(VO_2)(HL1^{open})(OH)]$, which explains why a high U(VI)/V(V) SF was achieved for PSZ-70/PSZ-60. A greater difference was observed in the closed state of HL1, with a ΔG of $[(UO_2)(HL1^{close})(OH)_3]^-$ 199.83 kJ·mol^{-1} lower than that of $[(VO_2)(HL1^{close})(OH)]$, which explains why the U(VI)/V(V) SF in the closed state was greater than that in the open state.

DFT simulations were further conducted to elucidate the detailed structure of PSZ-70. The optimized structure of PSZ-70-close (Fig. 5l) was characterized by holes that were enclosed by HL1, and the sizes of these holes coincided with the size of $[UO_2(CO_3)_3]^{4-}$. The radius of the hole, which is defined as the distance between the center of the hole and the closest atom in the MOF, is 4.51 Å. The radius of $[UO_2(CO_3)_3]^{4-}$, which is defined as the distance between U and the outmost atom in $[UO_2(CO_3)_3]^{4-}$, is 4.28 Å. Figure 5m shows that the optimized structure of $[UO_2(CO_3)_3]^{4-}$ overlapped exactly with the optimized structure of PSZ-70-close; this hole, by trapping $[UO_2(CO_3)_3]^{4-}$ in the closed state of PSZ-70, was responsible for the excellent uranium selectivity. Compared with that of $[UO_2(CO_3)_3]^{4-}$, the size of $[H_2VO_4]^-$ was significantly smaller. The radius of $[H_2VO_4]^-$ (the distance between V and the outmost atom in $[H_2VO_4]^-$) is 2.42 Å, which is short than the radius of the hole (4.51 Å). As shown in Fig. 5n, it was more difficult for PSZ-70-close to trap $[H_2VO_4]^-$ due to the size mismatch. Therefore, the precise trapping process of the uranium species in the as-prepared photoisomeric material was influenced by an immense spatial coordination effect, and conclusions can be drawn from the above adsorption results as well as from the outcomes of the above simulations on the pore behavior of the photoswitch monomers and the composites. Namely, $[UO_2(CO_3)_3]^{4-}$, which had a better geometrical match with the pore structure than the competitor $[H_2VO_4]^-$, was firmly bound inside the pore and thus strongly coordinated with the HL1 ligands, which accounted for the excellent separation of uranium and vanadium in the photoisomeric composites; this separation was possibly caused by the spatially confined conditions provided by the MOFs pores. Similarly, typical uranium-friendly amidoxime ligands exhibited less spatial directionality when complexed with uranium; thus, the precise capture of uranium could not be achieved in complicated seawater systems.

Methods

Characterizations

All scanning electron microscope (SEM) digital photograph were obtained from Thermo Scientific Apreo II SEM Field Emission Scanning Electron Microscope and Energy Dispersive X-Ray Spectroscopy (EDX) pattern of the measured elements were obtained utilizing EDAX GENESIS Series X-ray energy spectrometer. All samples involved need to be sprayed with gold for 120 s before testing. ^{1}H NMR were recorded on Bruker Avance NEO 400 MHz and 600 MHz NMR spectrometer using DMSO-d_6 with several drops Trifluoroacetic acid-d as the NMR solvent. The correspondence samples' spectra were calibrated against DMSO-d_6. Powder X-ray diffraction (PXRD) patterns were recorded on a Rigaku Corporation Combined Multifunctional X-Ray Diffractometer Ultima IV Series with a copper X-ray source and a scintillation counter detector. Samples were measured from 5 to 90 degrees in 2 theta using a scan speed of 15° 2 theta per minutes. Fourier infrared transform spectra (FT-IR) of samples were measured on a Bruker ALPHA Fourier Transform Infrared Spectrometer. All samples are prepared using the potassium bromide compression method. Data on the N_2 gas adsorption isotherm were gathered at 77 K on a Micromeritics ASAP 2460 Series Multi-Station Expanded Automatic Specific Surface and Pore Size Analyzer. All samples were degassed and held at 110 °C for 10 h.

UV-Vis absorbance spectroscopy was recorded on PerkinElmer Lambda 35 Ultraviolet Visible Spectrophotometer. Photo-heterostructured composites Diffuse Reflectance Spectroscopy (DRS)

https://doi.org/10.1038/s41467-025-57638-4

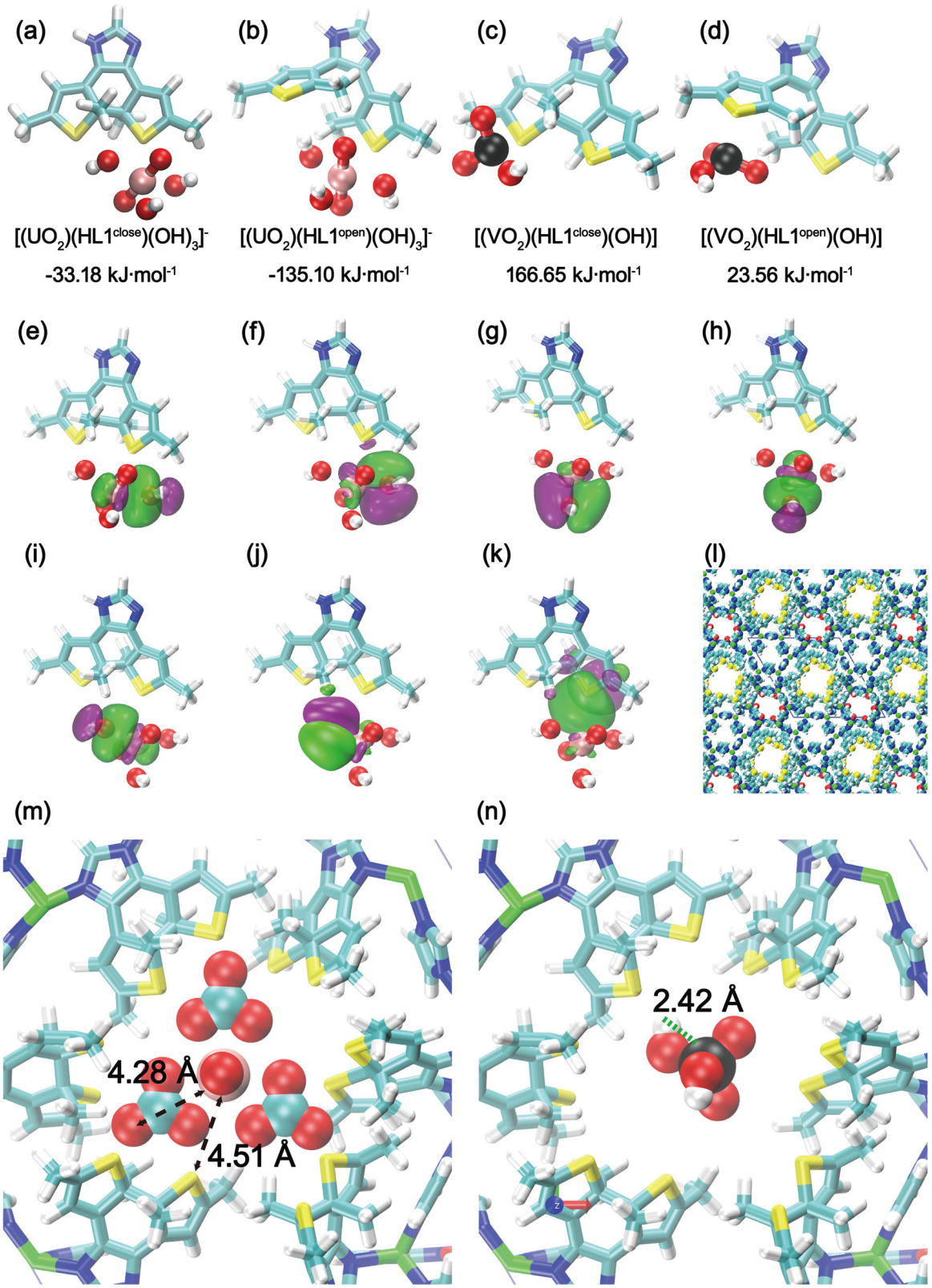

Fig. 5 | Separation mechanism of uranium by the photoisomerized MOFs. **a**–**d** Optimized complex structures formed by $HL1^{close}$ and UO_2^{2+}, $HL1^{open}$ and UO_2^{2+}, $HL1^{close}$ and VO_2^{+}, and $HL1^{open}$ and VO_2^{+} according to DFT simulations. **e**–**k** NBO orbitals between U and O in the hydroxyl group and between U and S in the dimethylthiophene group for the $[(UO_2)(HL1^{close})(OH)_3]^-$ complex. **l** Optimized structure of PSZ-70-close from DFT simulations. **m**, **n** Overlap of the optimized structure of $[UO_2(CO_3)_3]^{4-}$ with the optimized structure of PSZ-70-close, and overlap of the optimized structure of $[H_2VO_4]^-$ with the optimized structure of PSZ-70-close. H, C, N, O, S, U, V, and Zn atoms are shown in white, cyan, blue, red, yellow, pink, black, and green, respectively. The NBO orbitals are indicated by green and purple isosurfaces.

were measured with a UV–vis–NIR spectrometer (Varian Cary 5000), spectrally pure barium sulfate was used as a reference during the analysis. A Kratos AXIS UltraDLD equipment was used to carryout X-ray photoelectron spectroscopy (XPS) on the samples while employing an Al Kα radiation source at 10 kV and 5 mA.

Synthesis of ZIF-60, ZIF-70, PSZ-60 and PSZ-70

ZIF-60: Stir for an hour while sonicating 0.81 g (2.73 mmol) of $Zn(NO_3)_2{\cdot}6H_2O$ that has been dissolved in 90 mL of DMF solution. When the mixture was transparent, 0.54 g (7.95 mmol) of imidazole and 0.21 g (0.52 mmol) of 2-methylimidazole were added to the reaction system and stirred for 10 h at 85 °C. After the reaction was complete, the system was cooled to the room temperature, washed three times alternately with ethanol and DMF solution, and the resultant white powdered product was dried under vacuum.

ZIF-70: The Pyrex tube was filled with 0.2 g of $Zn(NO_3)_2{\cdot}6H_2O$, then 1 mL of DMF solution was carefully poured along the tube's wall and sonicated until the solution was clear and colorless. This cleared solution was then incorporated with 2.5 mL of DMF solution, 0.05 g (0.74 mmol) of imidazole, 83 mg (0.74 mmol) of 2-nitroimidazole, then sonicated one more to obtain a clarified yellow solution. Liquid nitrogen was used to freeze the system, and the Pyrex tube was sealed using internal evacuation and flame. The reaction system was created in batches, and then the sealed Pyrex tubes were subjected to a 4-day reaction at 120 °C. Following the reaction's termination, the glass tubes were allowed to cool naturally to room temperature. The products were then washed with DMF solution alternating with MeOH solution before being submerged in brand-new chloroform solution for further usage.

PSZ-60 and PSZ-70: The preparation of the two photoisomerized MOFs is identical, with the only difference being the MOFs substrate used in the reaction. The synthesized photoisomer HL1 was mixed with 50 mL of n-butanol solution and dissolved by ultrasonication, and a certain amount of ZIFs material was added and left at 120 °C for four days. Following the reaction, the system was cooled to room temperature, the remaining liquid in the reaction vessel was discarded, the product was washed three times with DMF while alternately washing with methanol solution, and the solid that resulted from the washing process was then freeze-dried for use in subsequent experiments.

Synthesis of DAE photoswitch (HL1)

A 1000 mL jacketed flask inside had nitrogen gas purged before reaction feeding. Mechanical stirring was used to mix enough $TiCl_4$ into 100 mL of dichloromethane, and an external low-temperature coolant circulation pump was adjusted at a temperature range of −15 to −5 °C. 1.8 mL (22.3 mmol) of pyridine and 5.076 mL (44.6 mmol) of 2,5-dimethylthiophene were added while maintaining a constant drop acceleration rate of half a drop every second using a constant pressure dropping funnel. The same dropping rate was used to add 2.285 mL (26.8 mmol) of oxalyl chloride following the addition of the reactants. The reaction temperature was set to −10 °C after the addition and maintained there for 4 h. The external coolant circulation was now stopped, and TLC (thin-layer chromatography) was used to track the reaction in real time. The reaction mixture was transferred to a separatory funnel to separate the organic layer after 250 mL of 0 °C deionized water was cautiously added to the flask in multiple pieces when the system temperature reached 0 °C. 150 mL of chloroform was used to extract the aqueous layer twice. The separated organic phases were then mixed, neutralized three times with deionized water, and washed with saturated sodium bicarbonate solution and saturated sodium chloride solution in that sequence. After using anhydrous sodium sulfate to dry the organic phase, the reddish-brown liquid was then obtained by filtering under reduced pressure, concentrated by spin evaporation, and then the product was separated from impurities using silica gel column chromatography with an 8:1 eluent mixture of hexane and ethyl acetate solution. Verification using thin-layer chromatography revealed that the R_f Value was 0.38. This is intermediate 1,2-bis-(2,5-dimethyl-thiophen-3-yl)-ethanedione.

Using the intermediate product from the above reaction as a guide, 25 mL of glacial acetic acid was added to the flask, then 2.875 g (37.3 mmol) of ammonium acetate was added while magnetic stirring was used. Finally, 450 mg of the intermediate product was added when the solution was lucid and transparent, and it was evenly dispersed throughout the system. The reaction system was then maintained at reflux for 48 h at 90 °C, adding 0.9 mL (37% w/w) of formaldehyde solution drop by drop. A little amount of off-white insoluble substance was formed when the reaction was finished, the system was cooled to room temperature, and 45 ml of deionized water was added. After that, the system was neutralized to pH=7 using ammonia, with the knowledge that there would be a further increase in the amount of insoluble material. The suspension system was put into a partition funnel, and the organic phase was extracted using 250 mL of dichloromethane in three steps. After that, it was washed with saturated sodium bicarbonate solution and saturated sodium chloride solution, dried with anhydrous sodium sulfate, and then filtered under reduced pressure to obtain an orange solution. Rotating evaporation was used to dry the solution, and once numerous off-white crystals had formed, a small amount of methyl tert-butyl ether was added and boiled. The final product, HL1 (4,5-bis(2,5-dimethyl-3-thienyl)-1H-imidazole), was then quickly filtered under decreased pressure. Yield: 0.14 g, 31% yield.

^{1}H NMR analysis of HL1/ZIF-70/PSZ-70/ZIF-60/PSZ-60

The samples to be tested were accurately weighed and dissolved using DMSO-d_6 with three drops of Trifluoroacetic acid-d, controlling the concentration of all samples to be 0.1 M. The MOFs materials before and after grafting with the photoisomer were tested using a Bruker Avance NEO 400 MHz and a Bruker Avance NEO 600 MHz, respectively.

The measured ^{1}H NMR spectra were baseline and phase corrected using MestRenova software, and then accurately analyzed by peak finding and integration. The proton peaks in the spectra were identified according to the chemical structure of the measured substances, and the MOFs were analyzed by the organic molecules contained in the structural building blocks. The grafting rate was determined using the peak area comparison method while controlling the sample concentration before and after the grafting photoswitch. Based on the differences and peculiarities of the chemical structure composition of the two MOFs materials, their grafting rates were calculated as shown below:

For PSZ-60:

$$\text{grafting ratio}\,(\%) = \frac{\text{Absolute value of the integral area}\,(\text{PSZ}-60-\delta(6.69))}{\text{Absolute value of the integral area}\,(\text{PSZ}-60-\delta(7.68))}$$

For PSZ-70:

$$\text{grafting ratio}\,(\%) = \frac{\text{Absolute value of the integral area}\,(\text{PSZ}-70-\delta(6.71))}{\text{Absolute value of the integral area}\,(\text{PSZ}-70-\delta(7.68))}$$

UV-Vis absorption spectroscopy study of HL1

In a 50 mL transparent quartz glass tube, correctly weigh 0.0018 g of HL1 monomer, pour 20 mL of CH_3OH along the tube's wall, and sonicate for 10 min to completely dissolve it. The prepared system was placed in the photochemical reactor with the magnetic stirring device, and the UV radiation was applied simultaneously with the stirring device being switched on. A UV-visible spectrophotometer was used to

measure the spectra in the 200–800 nm region after samples were obtained at the proper time intervals.

Study of UV-visible solid diffuse reflectance spectra of MOFs materials

An appropriate amount of sample was deposited on the quartz glass surface in the sample tray after the MOFs had been thoroughly ground, and the screw cap was tightened at the bottom to spread the sample out equally in the window. Spectra of samples between 200 nm and 800 nm were measured using $BaSO_4$ as a reference.

Adsorption in U-spiked simulated seawater

1 L of deionized water was used to dissolve 0.153 g of sodium bicarbonate and 25.6 g of sodium chloride. This solution was then sonicated for 24 h and stored in a sterile reagent container. The procedure used to set up the adsorption system was as follows: the amount of simulated seawater needed for the experiment was adjusted to pH=8.0 using 0.01 M NaOH and HCl, and then the simulated seawater, uranyl nitrate solution, and adsorbent suspension were added to the PE centrifuge tube in the appropriate quantity based on the differences in the adsorption experiment being investigated. To simulate the actual process of uranium extraction from seawater, we set the concentration of uranyl nitrate in the static adsorption study to be in the range of 0.8–4.8 ppm and the mass of the adsorbent involved to be 5 mg. The tubes were taken out from a constant temperature air bath shaker after 24 h and centrifuged at 12000 rpm. After adding a certain amount of supernatant, 0.5 M nitric acid solution, deionized water, and arsenazo (III) solution to a clean 20 mL glass vial, the solution's absorbance was measured at 652 nm by spectrophotometry after 20 min of color development. The data were measured and recorded.

pH-dependent uranium adsorption in U-spiked simulated seawater

According to the method for adjusting the pH of simulated seawater, the pH of the eight centrifuge tubes was set to 3, 4, 5, 6, 7, 8, 9, and 10, respectively, and the final uranium concentration was calculated in the same way. The behavior of the adsorption capacity of the material with pH can be obtained by using pH on the graph of uranium removal rate, where the uranium removal rate is expressed by the following equation:

$$\text{Uranium Removal Rate}\,(\%) = \frac{(C_0 - C_e)}{C_0} \times 100\%$$

Where C_0 ($mol{\cdot}L^{-1}$) is the actual initial concentration of uranium in each tube, C_e ($mol{\cdot}L^{-1}$) is the concentration of uranium in each tube at the moment of adsorption equilibrium.

Adsorption thermodynamics study in U-spiked simulated seawater

For the study of the thermodynamic behavior of the adsorption of MOFs substrates, several parallel experiments should be conducted, and error bars should be used to reflect the fluctuation of the data. The experimental data were fitted based on the following two adsorption models. One of them is the Langmuir adsorption model, and the specific mathematical expression is:

$$\frac{C_e}{q_e} = \frac{C_e}{q_m} + \frac{1}{k_a q_m}$$

Where C_e ($mg{\cdot}L^{-1}$) is the concentration at adsorption equilibrium in the tube, q_m ($mg{\cdot}g^{-1}$) is the maximum adsorption capacity of the material in the current system, and k_a is the correlation coefficient to characterize the binding ability of the material to uranium.

And the other one is the Freundlich adsorption model, which has the equation is:

$$\lg q_e = \lg k_b + \frac{1}{n}\lg C_e$$

Where n and k_b are the experiment-related empirical constants.

The experimental data were fitted to the two models at 300 K, and the result of the correlation coefficient R^2 was used to attribute the adsorption behavior of the materials. The maximum adsorption capacity of the adsorbent materials at the current temperature conditions was calculated using the corresponding adsorption isotherm equation.

Adsorption behavior of materials in two states of photoisomerization in U-spiked simulated seawater

In this section of the work, the design of the adsorption system in a simulated seawater environment was used to carry out the switching control of the two photoisomeric MOFs artificially utilizing external UV irradiation. This portion of the study is expected to investigate, in contrast to conventional static adsorption experiments, the impact of irradiation time on the degree of photoswitch closure, and then evaluate the retention capacity of uranium in the current closed state using the material's maximum adsorption capacity at the corresponding time.

After the instrument is protected from light, the suspension of adsorbent under UV irradiation is pipetted into a centrifuge tube in batches with a certain time gradient under magnetic stirring, and then simulated seawater and uranyl nitrate solution are added sequentially according to the arrangement of the adsorption system until the adsorption equilibrium is reached and then the absorbance of the solution is determined. It is important to remember that these steps must be carried out in complete darkness. By plotting C_e versus q_e, the adsorption capacity of the photoisomeric composites can be determined at different irradiation times.

Photoswitch fatigue test

In this section of the research on fatigue resistance, the adsorbent suspension was exposed to UV light for 15 minutes, and the system was taken out of the photochemical reflector as soon as a sample was taken. At this point it is placed in a visible light irradiated environment, after 20 minutes of exposure, we believe that the photoswitch has completely recovered from its initial closing conformation. Following this, the operation is repeated, with one UV-visible light sampling process being recorded as one cycle. Five cycles are then carried out to ensure the validity and consistency of the experimental data.

Study of selective adsorption behavior of materials in simulated seawater

In this section of the study, we investigated the open and closed state selective adsorption of two photoisomeric MOFs. We varied the concentrations of six elements—U, V, Cu, Fe, Ni, and Co—to 100 times the concentration found in natural seawater for the test out of convenience. The adsorption system was set up and placed in a constant temperature air bath shaker for 24 h before the determination of the metal elements using ICP-OES. The regulation of the photoswitch of the two materials was the same as the research methodology described above.

For the calculation of the material uranium-vanadium separation factor ratios, the following equations are to be referred to:

$$SF_{(U/V)} = \frac{K_d(U)}{K_d(V)}$$

The partition coefficients k for uranium and vanadium need to be accounted for concerning the initial concentration of the two substances in solution and the concentration after adsorption equilibrium,

and the results of the relevant concentration measurements have been given in Supplementary Table 4.

Stability testing of uranium/vanadium selectivity within the open-closed-open cycle of an in-situ modulated photoswitch

In contrast to selectivity studies of composite MOFs with defined open/closed conformations, the in-situ modulation process incorporates the effect of the solution system on the photoisomerization process, which is in principle difficult to predict trends in the change of its relevant properties. A polymetallic component system identical to the ion-selectivity experiments was prepared, and then a certain amount of adsorbent suspension was added for adsorption. Samples were taken at different time intervals under the irradiation of different external light sources, and the real-time changes in the ability of the materials to separate uranium and vanadium were determined using ICP-OES.

Adsorption in U-spiked natural seawater

Natural seawater from Ningde, Fujian Province, which was utilized in the studies, had to be isolated and filtered to get rid of any insoluble pollutants before use. The same uranium was spiked into three parallel sets of experiments at concentrations of 4, 6, 8, and 10 ppm, respectively. The photoisomerization of the adsorbent was controlled by maintaining the same solid-liquid ratio of the adsorbent in each PE tube to maintain control of the variables until the adsorption equilibrium was reached after 24 h. With respect to the backdrop of the corresponding uranium concentration, the material's maximal adsorption capacity was assessed spectrophotometrically.

Simulations and DFT calculations

The detailed COMSOL simulation methods and DFT calculation methods can be obtained in the supplementary information.

Data availability

All data supporting the findings of this study are available within the main text, supplementary information, and source data file. The source data of adsorption experiments and the atomic coordinates of the optimized computational models have been deposited in Figshare under accession code DOI link [https://doi.org/10.6084/m9.figshare.25293835].

References

1. Prelas, M. A. et al. A review of nuclear batteries. *Prog. Nucl. Energy* **75**, 117–148 (2014).
2. Seko, N. et al. Aquaculture of uranium in seawater by a fabric-adsorbent submerged system. *Nucl. Technol.* **144**, 274–278 (2003).
3. Maaz, M. et al. New insights on Uranium recovery from seawater and aqueous media. *Appl. Mater. Today* **18**, 100461 (2020).
4. Liu, P. et al. Recent advances in antibiofouling materials for seawater-Uranium extraction: a review. *Materials* **16**, 6451 (2023).
5. Das, S. et al. Novel poly(imide dioxime) sorbents: development and testing for enhanced extraction of uranium from natural seawater. *Chem. Eng. J.* **298**, 125–135 (2016).
6. Wang, D. et al. Significantly enhanced uranium extraction from seawater with mass produced fully amidoximated nanofiber adsorbent. *Adv. Energy Mater.* **8**, 1802607 (2018).
7. Djogic, R., Sipos, L. & Branica, M. Characterization of Uranium(VI) in seawater. *Limnol. Oceanogr.* **31**, 1122–1131 (1986).
8. Gunathilake, C. et al. Amidoxime-modified mesoporous silica for uranium adsorption under seawater conditions. *J. Mater. Chem. A* **3**, 11650–11659 (2015).
9. Wang, Z. et al. Multifunctional high boron content MOFs nano-co-crystals for precise boron neutron capture therapy for brain glioma in situ. *Nano Today* **45**, 101558 (2022).
10. Mo, Q. et al. Engineering single-atom sites into pore-confined nanospaces of porphyrinic metal-organic frameworks for the highly efficient photocatalytic hydrogen evolution reaction. *J. Am. Chem. Soc.* **144**, 22747–22758 (2022).
11. Chen, C. et al. Nanospace engineering of metal-organic frameworks through dynamic spacer installation of multifunctionalities for efficient separation of ethane from ethane/ethylene mixtures. *Angew. Chem. Int. Ed.* **60**, 9680–9685 (2021).
12. Zhang, S. et al. Stereoscopic 2D super-microporous phosphazene-based covalent organic framework: design, synthesis and selective sorption towards uranium at high acidic condition. *J. Hazard. Mater.* **314**, 95–104 (2016).
13. Yuan, Y. et al. A bio-inspired nano-pocket spatial structure for targeting uranyl capture. *Angew. Chem. Int. Ed.* **59**, 4262–4268 (2020).
14. Wang, W. et al. Structural and coordination microenvironment regulated MOF with phosphorylurea group to boost uranium adsorption. *Sep. Purif. Technol.* **346**, 127409 (2024).
15. Varsha, M. V. & Nageswaran, G. Review-2D layered metal organic framework nanosheets as an emerging platform for electrochemical sensing. *J. Electrochem. Soc.* **167**, 136502 (2020).
16. Song, Z. et al. Smart solvent-responsive covalent organic framework membranes with self-regulating pore size. *ACS Appl. Polym. Mater.* **5**, 3043–3054 (2023).
17. Mccarver, G. A. et al. Unraveling thermally regulated gating mechanisms in TPT pore-partitioned MOF-74: a computational endeavor. *Chem. Mater.* **36**, 8098–8106 (2024).
18. Mounfield, W. P., Iii & Walton, K. S. Effect of synthesis solvent on the breathing behavior of MIL-53(Al). *J. Colloid Interface Sci* **447**, 33–39 (2015).
19. Shi, Y.-X. et al. Guest-induced switchable breathing behavior in a flexible metal-organic framework with pronounced negative gas pressure. *Inorg. Chem.* **57**, 8627–8633 (2018).
20. Carrington, E. J. et al. Solvent-switchable continuous-breathing behaviour in a diamondoid metal-organic framework and its influence on CO_2 versus CH_4 selectivity. *Nat. Chem.* **9**, 882–889 (2017).
21. Fan, C. B. et al. Significant enhancement of C_2H_2/C_2H_4 separation by a photochromic diarylethene unit: a temperature- and light-responsive separation switch. *Angew. Chem. Int. Ed.* **56**, 7900–7906 (2017).
22. Uchida, K. et al. Photochromic crystalline systems mimicking biofunctions. *Chem. Eur. J.* **24**, 8491–8506 (2018).
23. Wu, J. et al. Photochromic inorganic-organic complex derived from low-cost deep eutectic solvents with tunable photocurrent responses and photocatalytic properties. *CrystEngComm* **22**, 1078–1085 (2020).
24. Kobatake, S. et al. Rapid and reversible shape changes of molecular crystals on photoirradiation. *Nature* **446**, 778–781 (2007).
25. Hnid, I. et al. Visualization and comprehension of electronic and topographic contrasts on cooperatively switched diarylethene-bridged ditopic ligand. *Nanomaterials* **12**, 1318 (2022).
26. Baggi, N. et al. Tuning the photochemical ring-closing reaction efficiency in diarylethene-based photoswitches through engineering of internal charge transfer. *Phys. Chem. Chem. Phys.* **25**, 7741–7749 (2023).
27. Yokojima, S. et al. Characterization of cationic diarylethene by electron spin resonance and absorption spectra - ratio of open/closed-ring isomers. *J. Phys. Chem. A* **110**, 8137–8143 (2006).
28. Lvov, A. G. et al. Photochromic diarylethene ligands featuring 2-(imidazol-2-yl)pyridine coordination site and their iron(II) complexes. *Beilstein J. Org. Chem.* **15**, 2428–2437 (2019).
29. Tan, W. et al. Near-infrared photochromic diarylethene iridium (III) complex. *Org. Lett.* **11**, 161–164 (2009).
30. Banerjee, R. et al. High-throughput synthesis of zeolitic imidazolate frameworks and application to CO_2 capture. *Science* **319**, 939–943 (2008).

31. Zhang, L. et al. Nickel metal-organic framework derived hierarchically mesoporous nickel phosphate toward smoke suppression and mechanical enhancement of intumescent flame retardant wood fiber/poly(lactic acid) composites. *ACS Sustain. Chem. Eng.* **7**, 9272–9280 (2019).
32. Hu, Z. et al. Direct synthesis of hierarchically porous metal-organic frameworks with high stability and strong bronsted acidity: the decisive role of hafnium in efficient and selective fructose dehydration. *Chem. Mater.* **28**, 2659–2667 (2016).
33. Manos, M. J. & Kanatzidis, M. G. Layered metal sulfides capture Uranium from seawater. *J. Am. Chem. Soc.* **134**, 16441–16446 (2012).
34. Patra, K. et al. Molecular models of atomically dispersed Uranium at mos2 surfaces reveal cooperative mechanism of water reduction. *J. Am. Chem. Soc.* **146**, 20147–20157 (2024).
35. Liu, Y. et al. Enhanced Uranium extraction via charge dynamics and interfacial polarization in mos2/go heterojunction electrodes. *Small* **20**, 2401374 (2024).
36. Zhang, D. et al. High-performance Photoelectrocatalytic Reduction of CO_2 by the hydrophilic-hydrophobic composite Cu-SnO_2/ZIF-8. *Int. J. Electrochem. Sci.* **16**, 150951 (2021).
37. Qi, Y. et al. Hydrophobic nanoporous silver with ZIF encapsulation for nitrogen reduction electrocatalysis. *Molecules* **28**, 2781 (2023).
38. Duan, H. et al. Tailoring stability, catalytic activity and selectivity of covalent metal-organic frameworks via steric modification of metal nodes. *J. Mater. Chem. A* **11**, 12777–12783 (2023).
39. Wei, X. et al. Ce-Modified flowerlike NiFe-MOF nanostructure based on ion competitive coordination for enhancing the oxygen evolution reaction. *Inorg. Chem.* **62**, 3238–3247 (2023).
40. Xu, S. et al. Precise molecular design for high-performance luminogens with aggregation-induced emission. *Adv. Mater.* **32**, 1903530 (2020).
41. Morimoto, M., Kobatake, S. & Irie, M. Multi-colored photochromic crystals of diarylethene mixtures. *Adv. Mater.* **14**, 1027–1029 (2002).
42. Kim, E. et al. Preparation and holographic recording of diarylethene-doped photochromic films. *ETRI J* **25**, 253–257 (2003).
43. Kang, H. et al. A new sensitive symmetric fluorescein-linked diarylethene chemosensor for Hg^{2+} detection. *J. Photochem. Photobiol. A Chem.* **367**, 465–470 (2018).
44. Ma, L. et al. Unsymmetrical photochromic bithienylethene-bridge tetraphenylethene molecular switches: Synthesis, aggregation-induced emission and information storage. *Chin. Chem. Lett.* **31**, 361–364 (2020).
45. Zuo, G. et al. Fabrication and characterization of Ag/AgCl@ZIF-8 hybrid nanostructure and used its as photocatalyst for degradation of rhodamine B under visible light. *J. Porous Mater.* **27**, 339–345 (2020).
46. Fu, Q.-T. et al. Diarylethene-based conjugated polymer networks for ultrafast photochromic films. *New J. Chem.* **43**, 15797–15803 (2019).
47. Mendoza, S. M. et al. Characterization by X-ray photoemission spectroscopy of the open and closed forms of a dithienylethene switch in thin films. *J. Phys. Chem. C* **111**, 16533–16537 (2007).
48. Li, W. et al. Self-assembled multilayers of alternating gold nanoparticles and dithiols: approaching to superlattice. *Colloids Surf. A Physicochem. Eng. Asp.* **175**, 217–223 (2000).
49. Xu, L. N. et al. Pendant thiol groups-attached Pd(II) for initiating metal deposition. *Appl. Surf. Sci.* **211**, 184–188 (2003).
50. Li, N., Xu, J. & Feng, R. Governing metal-organic frameworks towards high stability. *Chem. Commun.* **52**, 8501–8513 (2016).
51. Chen, X., Jiang, H. & Hou, B. Boosting chemical stability, catalytic activity, and enantioselectivity of metal-organic frameworks for batch and flow reactions. *J. Am. Chem. Soc.* **139**, 13476–13482 (2017).
52. Yang, F., Sadam, H. & Zhang, Y. A de novo sacrificial-MOF strategy to construct enhanced-flux nanofiltration membranes for efficient dye removal. *Chem. Eng. Sci.* **225**, 115845 (2020).
53. Wang, J., Zhang, M. & Zhai, J. Theoretical simulation of the ion current rectification (ICR) in nano-pores based on the Poisson-Nernst-Planck (PNP) model. *Phys. Chem. Chem. Phys.* **16**, 23–32 (2014).
54. Qian, S., Joo, S. W. & Ai, Y. Effect of linear surface-charge non-uniformities on the electrokinetic ionic-current rectification in conical nanopores. *J. Colloid Interface Sci.* **329**, 376–383 (2009).
55. Liu, T., Zhang, R. & Chen, M. Vertically aligned polyamidoxime/graphene oxide hybrid sheets' membrane for ultrafast and selective extraction of Uranium from seawater. *Adv. Funct. Mater.* **32**, 2111049 (2022).
56. Chen, X., Li, W. & Zhang, G. Highly stable and activated Cerium-based MOFs superstructures for ultrahigh selective uranium (VI) capture from simulated seawater. *Mater. Today Chem.* **23**, 100705 (2022).
57. Zhao, W., Li, L. & Liao, J. Regenerable and stable biomimetic hydroxyl-modified metal-organic frameworks for targeted uranium capture. *Chem. Eng. J.* **433**, 133787 (2022).
58. Peng, Y., Zhang, Y. & Tan, Q. Bioinspired construction of Uranium ion trap with abundant phosphate functional groups. *ACS Appl. Mater. Interfaces* **13**, 27049–27056 (2021).
59. Williams, D. E., Martin, C. R. & Dolgopolova, E. A. Flipping the switch: fast photoisomerization in a confined environment. *J. Am. Chem. Soc.* **140**, 7611–7622 (2018).
60. Cho, H. S., Yang, J. & Gong, X. Isotherms of individual pores by gas adsorption crystallography. *Nat. Chem.* **11**, 562–570 (2019).
61. He, W., Li, D. & Guo, S. Redistribution of electronic density in channels of metal-organic frameworks for high-performance quasi-solid lithium metal batteries. *Energy Storage Mater* **47**, 271–278 (2022).
62. Xin, Z., Wang, Y. & Chen, Y. Metallocene implanted metalloporphyrin organic framework for highly selective CO_2 electroreduction. *Nano Energy* **67**, 104233 (2020).
63. Liu, X., Qin, L. & Yu, Y. Light-Driven Handedness Inversion of Cholesteric Liquid Crystals. *Prog. Chem.* **35**, 247–262 (2023).
64. Hanikel, N., Pei, X. & Chheda, S. Evolution of water structures in metal-organic frameworks for improved atmospheric water harvesting. *Science* **374**, 454–459 (2021).
65. Zhang, J., Xu, S. & Wang, Z. Stimuli-responsive deep-blue organic ultralong phosphorescence with lifetime over 5 s for reversible water-jet anti-counterfeiting printing. *Angew. Chem. Int. Ed.* **60**, 17094–17101 (2021).
66. Zhou, J., Wang, S. & Zhang, J. Enhancing bioinspired aramid nanofiber networks by interfacial hydrogen bonds for multiprotection under an extreme environment. *ACS Nano* **17**, 3620–3631 (2023).
67. Cheng, H., Qiao, B. & Li, H. Protein-activatable diarylethene monomer as a smart trigger of noninvasive control over reversible generation of singlet oxygen: a facile, switchable, theranostic strategy for photodynamic-immunotherapy. *J. Am. Chem. Soc.* **143**, 2413–2422 (2021).
68. Park, J., Feng, D. & Yuan, S. Photochromic metal-organic frameworks: reversible control of singlet oxygen generation. *Angew. Chem. Int. Ed.* **54**, 430–435 (2015).
69. Schwartz, H. A., Laurenzen, H. & Kerschbaumer, S. High fatigue resistance of a photochromic dithienylethene embedded into the pores of a metal-organic framework (MOF). *Photochem. Photobiol. Sci.* **19**, 1730–1740 (2020).
70. Nie, H., Schauser, N. S. & Self, J. L. Light-switchable and self-healable polymer electrolytes based on dynamic diarylethene and metal-ion coordination. *J. Am. Chem. Soc.* **143**, 1562–1569 (2021).
71. Ao, J., Zhang, H. & Xu, X. A novel ion-imprinted amidoxime-functionalized UHMWPE fiber based on radiation-induced crosslinking for selective adsorption of uranium. *RSC Adv* **9**, 28588–28597 (2019).

72. Xu, M. Y., Han, X. L. & Hua, D. B. Polyoxime-functionalized magnetic nanoparticles for uranium adsorption with high selectivity over vanadium. *J. Mater. Chem. A* **5**, 12278–12284 (2017).
73. Zhang, L. X., Yang, S. & Qian, J. Surface ion-imprinted polypropylene nonwoven fabric for potential Uranium seawater extraction with high selectivity over vanadium. *Ind. Eng. Chem. Res.* **56**, 1860–1867 (2017).
74. Ma, L., Huang, C. & Yao, Y. Y. Self-assembled MOF microspheres with hierarchical porous structure for efficient uranium adsorption. *Sep. Purif. Technol.* **314**, 123526 (2023).
75. Xie, Y. H., Wu, Y. & Liu, X. L. Rational design of cooperative chelating sites on covalent organic frameworks for highly selective uranium extraction from seawater. *Cell Rep. Phys. Sci.* **4**, 101220 (2023).
76. Zhu, J. et al. Investigation of uranium (VI) adsorption by poly(dopamine) functionalized waste paper derived carbon. *J. Taiwan Inst. Chem. Eng.* **91**, 266–273 (2018).
77. Zhao, Z. W. et al. Defect controlled MOF-808 for seawater uranium capture with high capacity and selectivity. *J. Mol. Liq.* **367**, 120514 (2022).
78. Zhang, Y. Z. et al. Poly(amidoxime)-graft-magnetic chitosan for highly efficient and selective uranium extraction from seawater. *Carbohydr. Polym.* **301**, 120367 (2023).
79. Wu, M. B. et al. Wooden composite separators with ultrahigh uranium/vanadium selectivity and antibacterial property for capturing uranium from seawater. *Compos. Commun.* **32**, 101159 (2022).
80. Li, N. et al. High-capacity amidoxime-functionalized β-cyclodextrin/graphene aerogel for selective uranium capture. *Environ. Sci. Technol.* **55**, 9181–9188 (2021).
81. Xin, Q. et al. Enhanced performance in uranium extraction by the synergistic effect of functional groups on chitosan-based adsorbent. *Carbohydr. Polym.* **300**, 120270 (2023).
82. Cheng, G. et al. Extremely stable amidoxime functionalized covalent organic frameworks for uranium extraction from seawater with high efficiency and selectivity. *Sci. Bull.* **66**, 1994–2001 (2021).
83. Song, Y. et al. Nanospace decoration with uranyl-specific hooks for selective Uranium extraction from seawater with ultrahigh enrichment index. *ACS Cent. Sci.* **7**, 1650–1656 (2021).
84. Hu, Y. et al. Photochemically triggered self-extraction of uranium from aqueous solution under ambient conditions. *Appl. Catal. B Environ.* **322**, 122092 (2023).
85. Aihara, T. et al. Rate of adsorption of Uranium from seawater with a calix 6 arene adsorbent. *Sep. Sci. Technol.* **27**, 1655–1667 (1992).
86. Luan, X. F. et al. Theoretical insights on improving amidoxime selectivity for potential uranium extraction from seawater. *J. Phys. Chem. A* **126**, 406–415 (2022).
87. Wang, C. Z. et al. Complexation of vanadium with amidoxime and carboxyl groups: uncovering the competitive role of vanadium in uranium extraction from seawater. *Radiochim. Acta* **105**, 541–553 (2017).

Acknowledgements

Thanks to Prof. Jun Li at Tsinghua University for the valuable suggestions and assistance with DFT calculations. This work was supported by the National Natural Science Foundation of China (22176077, P.D.Q.; 22106058, W.F.); the Fundamental Research Funds for the Central Universities (lzujbky-2023-stlt01, P.D.Q.; lzujbky-2022-sp04, P.D.Q.); the Science and Technology Program of Gansu Province, China (23ZDFA014, P.D.Q.).

Author contributions

All authors have given approval to the final version of the manuscript. Z.P.C., P.D.Q., and W.W.S. conceptualized the project. Z.P.C. conducted the experimental work, analyzed the data, and drafted the initial manuscript. Z.Y.X., H.W.W., T.Z.W., and X.W.X. assisted in synthesizing photoswitch and composite MOFs. L.W. and C.S.W. assisted in analyzing the characterization results. W.F. and Z.P.C conducted the simulation and calculation work. W.F., W.Y.X. and P.D.Q. supervised the work.

Competing interests

The authors declare no competing interests.

Additional information

Supplementary information The online version contains supplementary material available at https://doi.org/10.1038/s41467-025-57638-4.

Correspondence and requests for materials should be addressed to Fei Wu, Yaxing Wang or Duoqiang Pan.

Peer review information *Nature Communications* thanks Subiao Liu, Shuyan Song, and the other, anonymous, reviewers for their contribution to the peer review of this work. A peer review file is available.

Reprints and permissions information is available at http://www.nature.com/reprints

Publisher's note Springer Nature remains neutral with regard to jurisdictional claims in published maps and institutional affiliations.

Open Access This article is licensed under a Creative Commons Attribution-NonCommercial-NoDerivatives 4.0 International License, which permits any non-commercial use, sharing, distribution and reproduction in any medium or format, as long as you give appropriate credit to the original author(s) and the source, provide a link to the Creative Commons licence, and indicate if you modified the licensed material. You do not have permission under this licence to share adapted material derived from this article or parts of it. The images or other third party material in this article are included in the article's Creative Commons licence, unless indicated otherwise in a credit line to the material. If material is not included in the article's Creative Commons licence and your intended use is not permitted by statutory regulation or exceeds the permitted use, you will need to obtain permission directly from the copyright holder. To view a copy of this licence, visit http://creativecommons.org/licenses/by-nc-nd/4.0/.

© The Author(s) 2025